

# 1        **Geometric accuracy assessment of coarse resolution satellite** 2        **data sets: a study based on AVHRR GAC data at the subpixel** 3        **level**

4        **Xiaodan Wu<sup>1,2</sup>, Kathrin Naegeli<sup>2</sup>, and Stefan Wunderle<sup>2</sup>**

5        <sup>1</sup>College of Earth and Environmental Sciences, Lanzhou University, Lanzhou 730000, China

6        <sup>2</sup>Institute of Geography and Oeschger Center for Climate Change Research, University of  
7        Bern, Hallerstrasse 12, CH-3012 Bern, Switzerland

8        Correspondence to: Xiaodan Wu (wuxd@lzu.edu.cn)

9        **Abstract:** AVHRR Global Area Coverage (GAC) data provide daily global coverage of  
10       the Earth, which are widely used for global environmental and climate studies. However, their  
11       geolocation accuracy has not been comprehensively evaluated due to the difficulty caused by  
12       onboard resampling and the resulting coarse resolution, which hampers their usefulness in  
13       various applications. In this study, a Correlation-based Patch Matching Method (CPMM) was  
14       proposed to characterize and quantify the geo-location accuracy at the subpixel level for  
15       satellite data with coarse resolution, such as AVHRR GAC dataset. This method is neither  
16       limited to landmarks nor suffers from errors caused by false detection due to the effect of mixed  
17       pixels caused by a coarse spatial resolution, and thus enables a more robust and comprehensive  
18       geometric assessment than existing approaches. Data of NOAA-17, MetOp-A, and MetOp-B  
19       satellites were selected to test the geocoding accuracy. The three satellites predominately  
20       present West shifts in the across-track direction, with average values of -1.69 km, -1.9 km, -  
21       2.56 km and standard deviations of 1.32 km, 1.1 km, 2.19 km for NOAA-17, MetOp-A, and  
22       MetOp-B, respectively. The large shifts and uncertainties are partly induced by the larger  
23       satellite zenith angles (SatZ) and partly due to the terrain effect, which is related to SatZ and  
24       becomes apparent in the case of large SatZ. It is thus suggested that GAC data with SatZ less  
25       than 40° should be preferred in applications. The along-track geolocation accuracy is clearly  
26       improved compared to the across-track direction, with average shifts of -0.7 km, -0.02 km, 0.96  
27       km and standard deviations of 1.01 km, 0.79 km, 1.70 km for NOAA-17, MetOp-A, and  
28       MetOp-B, respectively. The data can be accessed from <http://www.esa-cloud-cci.org/> (Stengel  
29       et al., 2017) and <https://ladsweb.modaps.eosdis.nasa.gov/> (Didan, 2015).

## 30        **1 Introduction**

31        Advanced Very High Resolution Radiometer (AVHRR) data provide valuable data sources  
32        with a near daily global coverage to support a broad range of environmental monitoring  
33        researches, including weather forecasting, climate change, ocean dynamics, atmospheric

34 soundings, land cover monitoring, search and rescue, forest fire detection, and many other  
35 applications (Van et al., 2008). The unique advantage of AVHRR sensors is their long history  
36 dating back to the 1980s and thus enabling long-term analyses at climate-relevant time scales  
37 that cannot be covered by other satellites. However, AVHRR data are rarely used at the full  
38 spatial resolution for global monitoring due to the limited data availability (Pouliot et al., 2009;  
39 Fontana et al., 2009). Instead, the Global Area Coverage (GAC) AVHRR dataset with a reduced  
40 spatial resolution is generally employed in long-term studies at a global or regional perspective  
41 (Hori et al., 2017; Delbart et al., 2006; Stöckli et al., 2004; Moulin et al., 1997).

42 However, there are several known problems with the geo-location of AVHRR GAC data,  
43 which have a profound impact on their application. (1) The drift of the spacecraft clock results  
44 in errors in the along-track direction (Devasthale et al., 2016). Generally, an uncertainty of 1  
45 second approximately induces an error of 8 km in this direction. (2) Satellite orientation and  
46 position uncertainties influence the projection of the satellite geometry to the ground, which  
47 leads to errors in both along-track and across-track directions. (3) Earth surface elevation  
48 aggravates distortions in the across-track direction (Fontana et al., 2009). Without navigation  
49 corrections, the spatial misplacement of the GAC scene caused by these factors can be up to  
50 25-30 km occasionally (Devasthale et al., 2016).

51 For geocoding of AVHRR data, a two-step approach is usually used: 1) geocoding based  
52 on orbit model, ephemeris data, and time of onboard clock (Van et al., 2008), achieving an  
53 accuracy within 3-5 km depending on the accuracy of orbit parameters and model (Khlopenkov  
54 et al., 2010); 2) using any kind of ground control points (GCPs) (e.g., road or river intersections,  
55 coastal lines) to improve geocoding (Takagi, 2004; Van et al., 2008). Additionally, in order to  
56 eliminate the ortho-shift caused by elevations, an orthorectification would be needed (Aguilar  
57 et al., 2013; Khlopenkov et al., 2010). The dataset used in this study is from the ESA (European  
58 Space Agency) cloud CCI (Cloud Climate Change Initiative) project, which has corrected clock  
59 drift errors by coregistration of AVHRR GAC data with a reference dataset, and showed  
60 improved navigation by fitting the data to coastal lines.

61 Unlike the Local Area Coverage (LAC) data with a full spatial resolution of AVHRR, GAC  
62 data are sampled on board the satellite in real-time to generate coarser resolution data (Kidwell,  
63 1998). This is achieved by averaging values from four out of five pixel samples along a scan  
64 line and eliminating two out of three scan lines, resulting in a spatial resolution of  $1.1 \text{ km} \times 4$   
65  $\text{km}$  along the scan line with a 3 km distance between pixels across the scan line. Therefore, the  
66 nominal size of a GAC pixel is  $3 \text{ km} \times 4.4 \text{ km}$ . It is important to note that the spatial resolution  
67 of GAC data also depends on the satellite zenith angle (SatZ). Because of the large swath width,  
68 the spatial resolution of LAC decreases to 2.4km by 6.9 km at the edge of the swath (D'Souza  
69 et al., 1994). With the selection process for GAC, the GAC resolution is also much worse than  
70 4 km. Furthermore, the onboard resampling process of GAC data makes the orthorectification  
71 not feasible, which results in lowering of geolocation accuracy in the across-track direction.  
72 The final quality of AVHRR GAC data has not been quantified and we, therefore, make an

73 attempt to assess their geolocation accuracy, particularly over terrain areas.

74 There are generally three approaches to assess the non-systematic geometric errors of  
75 satellite images: (1) the coastline crossing method (CCM) which detects the coastline in the  
76 along-track and across-track directions through a cubic polynomial fitting (Hoffman et al.,  
77 1987); (2) the land-sea fraction method (LFM) which develops a linear radiance model as a  
78 function of land-sea fraction, land and sea radiance, and then finds the minimum difference  
79 between model-simulated and instrument-observed radiance by shifting the pixels in along-  
80 track and across-track directions (Bennartz, 1999); (3) the coregistration method which  
81 computes the difference or similarity relative to a reference image (Khlopenkov et al., 2010).  
82 The abilities of these three methods in characterizing the geometric errors are limited and  
83 dependent on different, method-dependent factors. Whereas, the CCM is subject to the structure  
84 of coastline, and the LFM depends on the accuracy of the land-sea model but shows advantages  
85 on complex coastlines (Han et al., 2016). The coregistration method is usually applied to high-  
86 resolution visible and infrared images (Wang et al., 2013; Wolfe et al., 2013) as it relies on  
87 individual objects/landmarks in both datasets. However, when it comes to coarse resolution  
88 data with several kilometers' pixel size, the main difficulties arise from false detection due to  
89 the effect of mixed pixels, which hampers the application of the existing methods. An approach  
90 assessing the geolocation accuracy of coarse resolution satellite data is thus strongly needed.  
91 The geometric accuracy is important as even small geometric errors can lead to significant  
92 noises on the retrieval of surface parameters, such as NDVI, LAI, and albedo, which mask the  
93 reality or bias the final results and conclusions (Khlopenkov et al., 2010; Arnold et al., 2010).  
94 For instance, anomalous NDVI dynamics during the regeneration phase of forest fire-burnt  
95 areas can be explained by the imprecise geolocation of the data set used (Alcaraz-Segura et al.,  
96 2010). Therefore, it is critical to develop a rigorous geometric accuracy assessment method in  
97 order to ensure the effectiveness of AVHRR GAC data in the generation of climate data records  
98 (CDR) (Khlopenkov et al., 2010; Van et al., 2008).

99 Based on the idea of the coregistration method, this study proposes a method named  
100 Correlation-based Patch Matching Method (CPMM), which is capable of quantifying the  
101 geometric accuracy of coarse resolution satellite data available as fundamental climate data  
102 records (FCDR) for global applications (Hollmann et al., 2013). We show the procedure based  
103 on AVHRR GAC data, which are compiled for the ESA CCI cloud project (Stengel et al., 2017)  
104 and are now also used for the ESA CCI+ snow project. The assessment is conducted at the sub-  
105 pixel level and not affected by the mixed pixel problem. This method is tested using satellite  
106 data from NOAA-17, MetOp-A, and MetOp-B, respectively. Furthermore, the potential factors  
107 that cause geometric distortions are explored and discussed. Although the band-to-band  
108 registration (BBR) accuracy assessment is an important aspect for such multi-spectral images,  
109 it is not a focus of this study, since the BBR accuracy of AVHRR has been comprehensively  
110 evaluated by a previous study (Aksakal et al., 2015).

## 111 2 Data and geographical regions of interest

### 112 2.1 Satellite data

113 AVHRR is a multipurpose imaging instrument aboard on the NOAA satellite series since  
114 1978 and the Meteorological Operational Satellites (MetOp) operated by EUMETSAT since  
115 2006, delivering daily information of the Earth in the visible, near-infrared, and thermal  
116 wavelengths. They provide observations from 4 to 6 spectral bands, depending on the  
117 generation of AVHRR sensors. This study only focuses on the AVHRR GAC data observed by  
118 NOAA-17 (AVHRR-3 generation), MetOp-A, and MetOp-B. The spectral characteristics of the  
119 AVHRR sensors on board these three platforms are the same and summarized in Table 1. Since  
120 the spatial resolution of AVHRR GAC data is often considered to be 4 km (Fontana et al., 2009),  
121 the analysis in this study was conducted at the 4 km level using the data acquired on August 13,  
122 2003 for NOAA-17 and March 12, 2017 for MetOp-A and MetOp-B.

123 **Table 1.** Spectral characteristics of AVHRR sensors

Band	Wavelength ( $\mu\text{m}$ )	Application
1	0.58–0.68 (VIS)	Cloud mapping, vegetation and surface characterization
2	0.72–1.00 (NIR)	Vegetation mapping, water body detection
3a*	1.58–1.64 (MIR)	Snow and Ice classification
3b*	3.55–3.93 (MIR)	Cloud detection, Sea/Land surface temperature,
4	10.30–11.30 (TIR)	Cloud detection, Sea/Land surface temperature,
5	11.50–12.50 (TIR)	Cloud detection, Sea/Land surface temperature

124 \*Note: Channel 3a is only used continuously on NOAA-17 and MetOp-A. On-board MetOp-B channel 3a was only  
125 active during a limited time span.

126 From a standpoint of geometric accuracy assessment, the reflectances in band 1 and 2 were  
127 employed in this study. However, these two bands are not only affected by the atmosphere but  
128 also by the earth surface anisotropy characterized by the bidirectional reflectance distribution  
129 function (BRDF) (Cihlar et al., 2004). Given the fact that BRDF effects can be reduced through  
130 the calculation of vegetation indices such as NDVI (Lee & Kaufman, 1986), the NDVI is  
131 employed in this study, which is derived from the reflectance in band 1 and 2 according to  
132 Equation (1).

$$133 \quad NDVI = \frac{R_2 - R_1}{R_2 + R_1} \quad (1)$$

134 where  $R_1$  and  $R_2$  refer to the reflectance in band 1 and 2, respectively. It is important to note  
135 that during the process of generating NDVI, the atmospheric and BRDF corrections were not  
136 performed. But it is expected that such effects originating from these omissions are of minor  
137 influence, because the method of this study is based on correlation analysis and does not rely

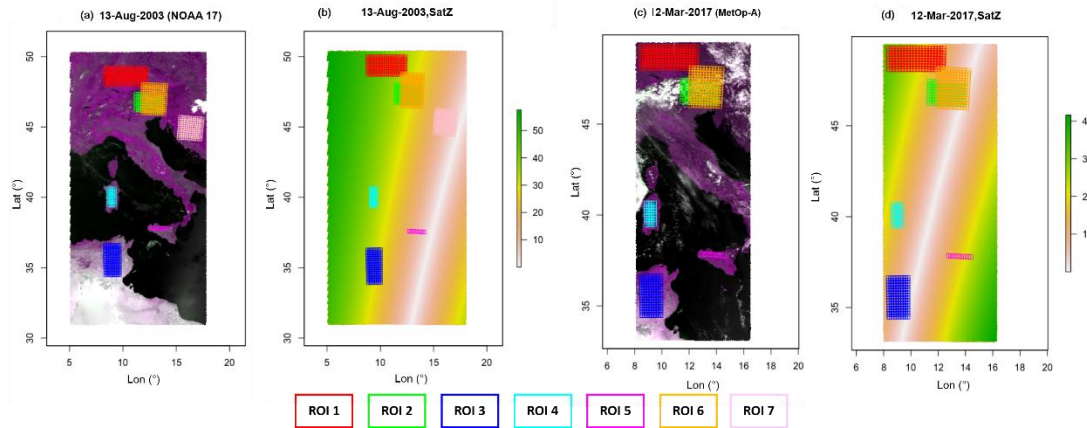
138 on absolute values of NDVI. Another advantage of using NDVI is that it has higher contrast  
139 between different land cover types, such as vegetation/no-vegetation, snow/no-snow, etc.  
140 Furthermore, in order to investigate the effect of off-nadir viewing angle on geometric accuracy,  
141 the SatZ data of AVHRR were also extracted.

142 Ideally, the referenced data in geometric quality assessment should meet the required  
143 accuracy of 1/3 field of view (FOV) (WMO and UNEP, 2006), and also satisfy the accuracy  
144 requirement of an order of magnitude better than one-tenth of the image spatial resolution  
145 (Aksakal, 2013), which means 400 m for the AVHRR GAC data. The NDVI provided by  
146 MOD13A1 V006 product was introduced as a source of reference data to perform the geometric  
147 quality assessment, because the sub-pixel accuracy of MODIS product is sufficient to satisfy  
148 this requirement (Wolfe et al., 2002). The high geolocation accuracy of MODIS products was  
149 achieved by using the most advanced data processing system, which has updated the models of  
150 spacecraft and instrument orientation several times since launch. Consequently, the various  
151 geolocation biases resulted from instrument effects and sensor orientation are removed (Wolfe  
152 et al., 2002). The NDVI data with the date corresponding to that of AVHRR GAC data, were  
153 obtained from the Level-1 and Atmosphere Archive & Distribution System (LAADS)  
154 Distributed Active Archive Center (DAAC) (<https://ladsweb.modaps.eosdis.nasa.gov/>) with  
155 the sinusoidal projection at a spatial resolution of 500 m and a temporal resolution of 16-day.  
156 The detailed description of the MOD13A1 V006 product can be found in Didan (2015).

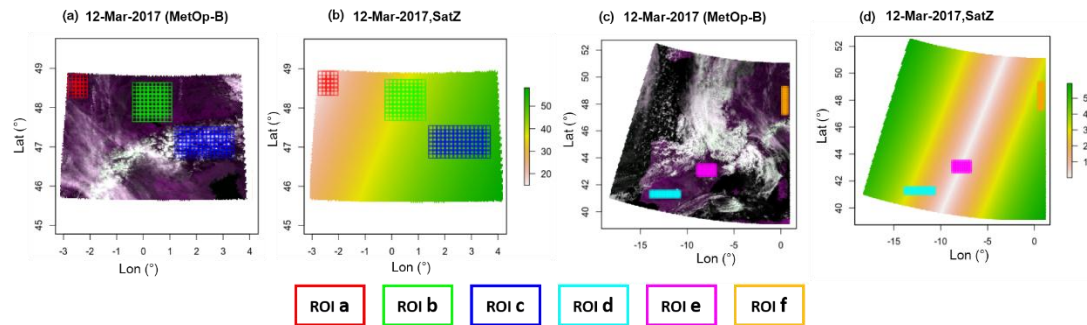
## 157 **2.2 Geographical regions of interest**

158 The purpose of this study is not only to assess the geolocation accuracy of 4 km AVHRR  
159 GAC data, but also to explore the potential impact factors related to geolocation accuracy.  
160 Therefore, the investigations were made at different latitudes and longitudes, at different  
161 locations with different SatZ, for different land covers, as well as different topographies. The  
162 swaths covering parts of Europe (including the alpine mountain) and Africa were used since  
163 they fit the study needs (Fig. 1). Investigations were based on six regions of interest (ROI) as  
164 shown in Figs. 1 and 2. The ROIs from 1 to 6 enable us to investigate the geolocation accuracy  
165 at different SatZ, topography, as well as latitudes and longitudes. Their locations and extents  
166 are consistent for the scenes from NOAA-17 and MetOp-A (Fig. 1), which enables the  
167 comparison of geolocation accuracy between these two sensors. The size of ROI was attempted  
168 to be set as large as possible in order to get more significant and comprehensive results. On the  
169 other hand, areas covered by cloud and water have to be avoided, resulting in the different sizes  
170 of these ROIs. Half of the ROIs (ROIs 2, 4, 6) serve as a good example for a typical  
171 mountainous areas on Earth. The other half of ROIs (ROIs 1, 3, 5), on the other hand, mainly  
172 cover relatively flat areas. Since the NOAA-17 scene was almost unaffected by cloud, another  
173 ROI (ROI 7) was selected to check the geolocation accuracy at nadir. The MetOp-B scene was  
174 influenced by cloud but served as a good example to illustrate the combined effect of  
175 topography and large SatZ (Fig. 2). Although there are also 6 ROIs (ROIs (a-f)) selected, their

176 sizes and extents are totally different from the above two scenes. In order to include the terrain  
 177 area, two subsets were used (Figs. 2a and c). Each grid in the ROI represents the minimum unit  
 178 (namely the patch) based on which we conduct the geometric quality analysis.



179  
 180 **Figure 1.** The study area and the distribution of ROIs. (a) and (c) are the composite maps of bands 2-1-  
 181 1 of AVHRR GAC data on August 13, 2003 and March 12, 2017, respectively. (b) and (d) are their  
 182 corresponding SatZ respectively, which is indicated by the color bar, with the white line representing  
 183 small SatZ along the satellite path.

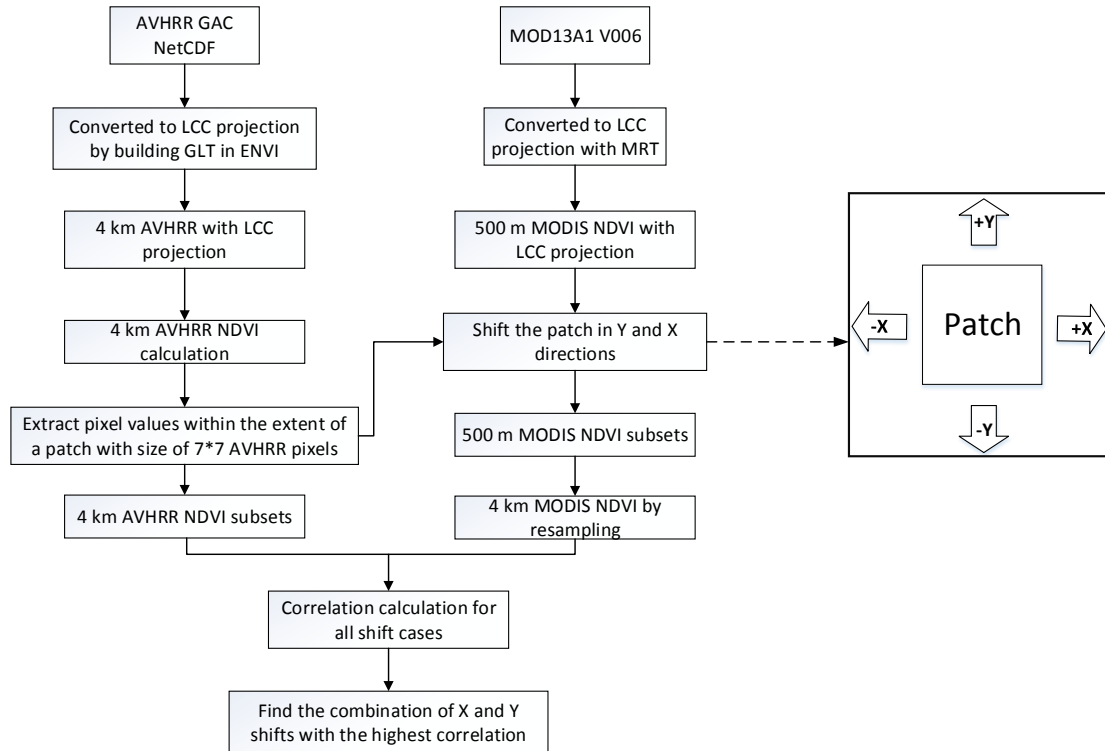


184  
 185 **Figure 2.** The study area and the distribution of ROIs on March 12, 2017. (a) and (c) are the composite  
 186 maps of bands 2-1-1 subset 1 and 2, respectively. (b) and (d) are their corresponding SatZ (indicated by  
 187 the color bar), respectively. The white line in (d) represents small SatZ along the satellite path.

### 188 3 Methodology

189 The assessment was performed by comparing the AVHRR GAC scenes with geo-located  
 190 reference data, i.e. MOD13A1 (V006). An approach named Correlation-based Patch Matching  
 191 Method (CPMM) is proposed to find the best match between small image patches taken from  
 192 the reference images and the AVHRR GAC images. This method is expected to be more suitable  
 193 for the geometric accuracy assessment of coarse resolution images than the current methods,  
 194 i.e. the CCM, LFM, and co-registration using shorelines. The framework of CPMM is shown  
 195 in Fig. 3, and the detailed description of this method is provided below.





196  
197 **Figure 3.** Flowchart of the Correlation-based Patch Matching Method (CPMM).

198 **3.1 Satellite data processing**

199 The AVHRR GAC data set is stored in a Network Common Data Format (NetCDF), with  
200 latitude and longitude assigned to each pixel. In order to achieve a higher accuracy of image  
201 matching, the data need to be reprojected. The AVHRR GAC scene was reprojected into the  
202 Lambert Conformal Conic (LCC) projection by building the Geographic Lookup Table (GLT)  
203 using the latitude and longitude data in ENVI. The spatial resolution of the AVHRR GAC map  
204 in the LCC projection is 4 km. Based on the reprojected data, the NDVI was calculated using  
205 the band combinations as indicated by Eq. (1). Similarly, the NDVI band of MOD13A1 in the  
206 HDF format was extracted and converted to LCC projection from its raw sinusoidal projection  
207 using the MODIS Reprojection Tool (MRT). The nearest neighbor (NN) resampling scheme  
208 was employed in this procedure. The spatial resolution of the MODIS NDVI in the LCC  
209 projection is 500 m. Thus, the geometric assessment is performed at the 4 km resolution of  
210 AVHRR NDVI based on the 500 m MODIS NDVI data.

211 **3.2 Patch matching and geometric assessment**

212 In the process of matching the AVHRR GAC data with reference MODIS data, a patch  
213 size of  $7 \times 7$  AVHRR pixels (corresponding to approximately  $28 \text{ km} \times 28 \text{ km}$ ) was used. These  
214 patches were distributed in each ROI as shown in Figs. 1 and 2, with an interval of 4 pixels in  
215 the along-track (Y-) and across-track (X-) direction. The sizes of the patch and interval were  
216 determined based on the following aspects: the size of the patch should contain enough pixels  
217 to support a robust correlation estimation, but at the same time, should not be too large in order

218 to investigate the potential influencing factors related to the geometric accuracy, and get enough  
219 results from these patches to attain a more significant and comprehensive conclusion. Similarly,  
220 the size of the interval should enable the disparity between different patches on one hand and  
221 on the other hand a large number of patches within the extent of each ROI. The chosen size has  
222 proven to be most ideal for these criteria during the test of different patch size.

223 For each patch in the ROI, the AVHRR GAC data within the patch were extracted. Then  
224 the patch was shifted in the Y- and X-direction as indicated by the arrows in Fig. 3. Shifts were  
225 conducted stepwise in order to achieve sub-pixel accuracy, beginning with only 500 m and  
226 adding up to 8 km (i.e.,  $\pm 2$  pixels) at a step of 500 m (equivalent to the MODIS pixel size) in  
227 any direction of Y- and X-combination. Consequently,  $33 \times 33$  combinations of X- and Y-shifts  
228 have been simulated. For each simulated shift, the MODIS NDVI pixels within the extent of  
229 the patch were extracted and aggregated to 4 km by spatial averaging. Afterwards, the  
230 correlation between the 4 km rescaled MODIS NDVI and the 4 km AVHRR NDVI was  
231 calculated for each shift in X- and Y-direction. The displacement of one patch was indicated by  
232 the shift combination with the best correlation, which means the geolocation accuracy of the  
233 patch. In this way, the geolocation errors were transformed into the across-track and along-track  
234 directions at the sub-pixel level for correlation with possible error sources.

235 It is expected that the results from each patch are different. Therefore, the general accuracy  
236 of each ROI was determined by summarizing the measured shifts of each respective patch  
237 statistically. Here, the histogram was employed to show the distribution of geometric errors in  
238 the across-track and along-track directions. And the quantitative indexes, such as the number  
239 of patches, their mean and standard errors, were calculated. The averaging is expected to reduce  
240 the uncertainties caused by random factors and produce accurate shift measurement estimates  
241 (Bicheron et al., 2011). The final shifts of the scene were calculated by averaging the measured  
242 shifts of all patches on the scene.

### 243 **3.3 Influence factor**

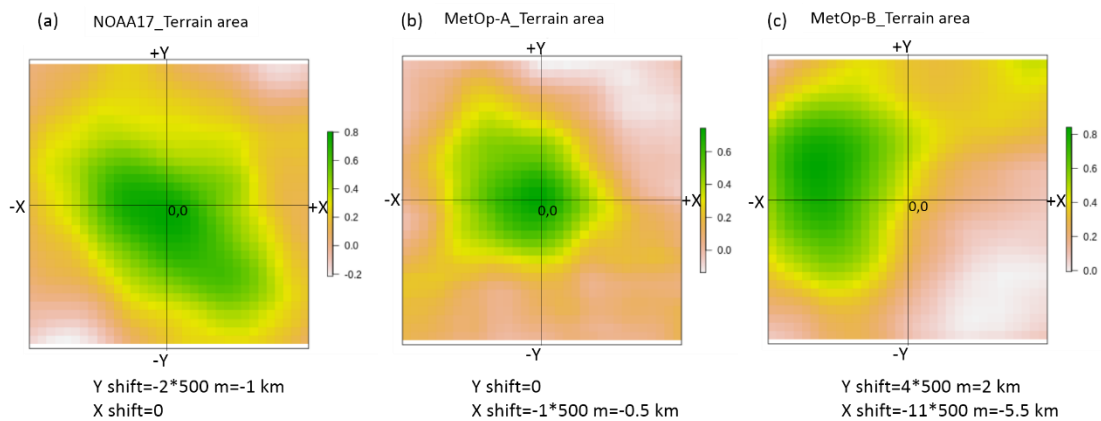
244 The influence of potential variables on the geometric accuracy was studied, including  
245 SatZ, topography, latitudes, and longitude. To achieve this, the information of these factors were  
246 also extracted for each patch on the scene. The geometric errors induced by SatZ were  
247 highlighted by checking the relationship between errors and SatZ. The effect of topography  
248 was investigated by checking the relationship of geometric errors in the across-track direction  
249 over terrain areas compared to relatively flat areas. The effect of latitudes and longitude was  
250 determined by analyzing their relationship with measured shifts on the along-track and across-  
251 track directions, respectively.

## 252 **4 Results and discussions**

253 Fig. 4 shows the correlation distribution over the  $33 \times 33$  simulated shifted cases within  $\pm$   
254 8 km range at a step change of 500 m. Here, only one patch is extracted from each respective



255 scene to illustrate the results. Each grid in Fig. 4 represents a shift combination case, which is  
 256 indicated by the location of the grid away from the center. The center of each subfigure depicts  
 257 the case in which the location of the patch on the reference scene is exactly overlapped with  
 258 that on the AVHRR scene. The results are visualized for one example showing the spatial  
 259 distribution of correlation between the MODIS reference scene and the AVHRR data (Fig. 4).  
 260 The color coding indicates a high correlation in dark green and reddish-white colors indicate  
 261 low correlation values. It can be seen that the correlation appears a maximum at a certain  
 262 location, and then becomes gradually smaller with increasing distance from that location. The  
 263 location with the maximum correlation indicates the actual displacement of this patch. Then the  
 264 geolocation errors can be transferred into distances in kilometer (km) by multiplying the  
 265 location of the grid with 500 m. An almost perfect match is shown in Fig. 4b, where the dark  
 266 green area is nearly centered at the coordinates (0, 0). From Fig. 4a, it can be found that the  
 267 patch on the NOAA-17 scene shows geolocation errors of -1 km and 0 km in the along-track  
 268 and across-track directions, respectively. The Fig. 4b indicates a geolocation error of 0 km and  
 269 -0.5 km in the along-track and across-track directions respectively for the patch on the MetOp-  
 270 A scene. And Fig. 4c indicates that the patch on the MetOp-B scene shows a geometric error of  
 271 2 km in the along-track direction and -5.5 km in the across-track direction. However, these  
 272 figures show only the results of one single patch. The final results are based on a large number  
 273 of samples to be statistically significant.



274

275 **Figure 4.** Variations of the correlation with respect to each shift combination. Only the results of one  
 276 patch from the NOAA-17 (left), MetOp-A (middle), and MetOp-B (right) scenes are shown for  
 277 conciseness.

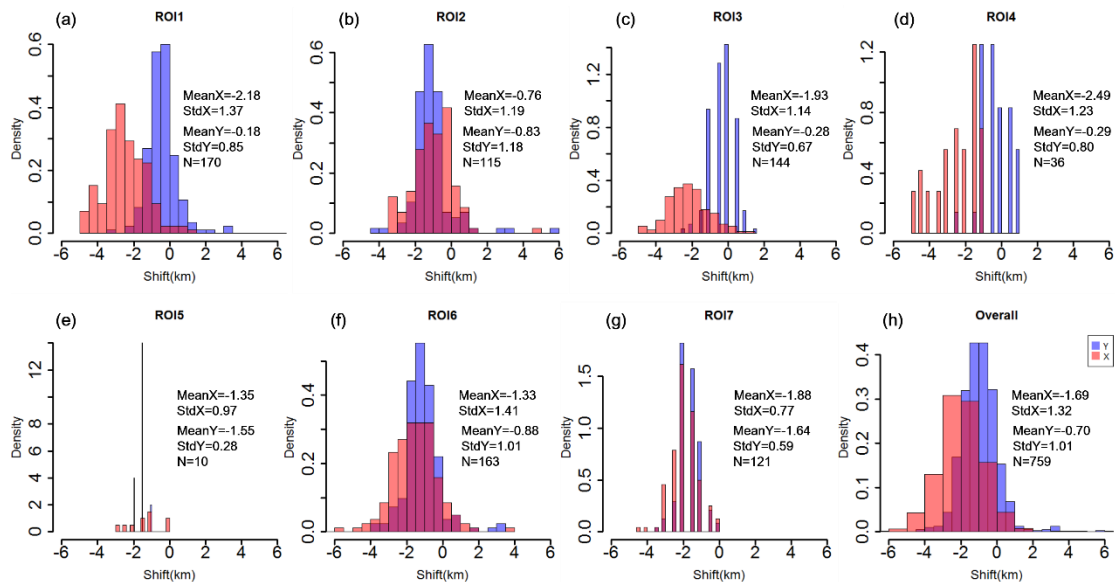
#### 278 4.1 Geocoding accuracy

279 The geolocation shifts of each patch are slightly different as shown in Figs. 5-7. The +y  
 280 indicates a shift to the North and +x indicates a shift to the East (minus sign indicates opposite  
 281 directions). The statistical indicators such as the mean value of shift (Mean), the standard  
 282 deviation of shift (StdDev) and the number of patches (N), are derived from the estimated shift  
 283 values of all patches within the extent of the corresponding ROI.

284 As shown in Fig. 5, it can be seen that the scene of NOAA-17 generally shows West shifts

285 in the across-track direction, since the majority of patches in all ROIs show negative shifts.  
 286 Nevertheless, the magnitudes of shifts for different ROIs vary from one to another. ROI 2 shows  
 287 the smallest shift with a mean value of -0.76 km, with most shifts concentrated around -1 (Fig.  
 288 5b). The ROIs 6 and 5 indicate the second smallest shifts, with still weak magnitudes of -1.33  
 289 and -1.35, respectively. Most of their shifts are distributed between -2 and 0 (Figs. 5f and e).  
 290 The ROIs 7, 3, 1, 4 show slightly larger mean shifts but are still with the magnitudes of less  
 291 than 2.5 km. These results are unexpected, because the ROIs (ROIs 2 and 6) over terrain areas  
 292 are with smaller shifts than those (ROIs 7, 3, 1, 4) over relatively flat areas in the across-track  
 293 direction. One possible reason is that the SatZ for ROIs 2 and 6 are not large (less than 40°)  
 294 (Fig. 1b) so that the terrain effect on geolocation accuracy is counterbalanced by the small SatZ.  
 295 This also indicates that the influence of small SatZ may be stronger than the terrain effect. But  
 296 it is surprising that the ROI 7 (Fig. 5g), which is located at the nadir area (Fig. 1b), shows even  
 297 larger shifts than other ROIs (ROIs 2, 6 and 5) with relatively larger SatZ. On the other hand,  
 298 ROI 7 shows the most stable behavior, indicated by the smallest StdDev of 0.77. Other ROIs  
 299 present relatively large, but still acceptable variations with StdDev ranging from 0.97 to 1.41  
 300 (Figs. 5a-g).

301 When combining the results of all ROIs together (Fig. 5h), the shifts in the across-track  
 302 direction generally follow an approximately normal distribution with a mean value of -1.69 and  
 303 a standard deviation of 1.32. Nearly 91% of the shifts are within the range of  $\pm 3$  km, and the  
 304 great majority (97%) of the shifts lay within a range of  $\pm 4$  km. The number of patches (N=759)  
 305 is assumed to be sufficient to ensure reliability and robustness of the results and the reduction  
 306 of the influence of random factors.



307

308 **Figure 5.** The distribution of shifts in the across-track (X, represented by red histogram) and along-track  
 309 (Y, denoted as blue histogram) directions over different regions for NOAA-17 scene. The unit of the  
 310 shift is km. For histograms, the heights of the bars indicate the density. In this case, the area of each bar  
 311 is the relative frequency, and the total area of the histogram is equal to 1.

312 The shifts in the along-track direction are mainly negative throughout these ROIs,  
 313 indicating that the NOAA-17 scene is dominated by South shifts in the along-track direction.  
 314 Nevertheless, a considerable number of patches also show slight North shifts over ROIs 1, 3  
 315 and 4 (Figs. 5a, c and d), where the shifts are distributed around 0 with mean values of -0.18, -  
 316 0.28 and -0.29, respectively. These shifts are generally small in these three regions given that  
 317 the maximum shift is no more than 3.5 km (Table 2). In contrast, the ROIs 2, 5, 6 and 7 present  
 318 systematic shifts to the South, which are mostly distributed within the range of -2 to 0 km, with  
 319 mean values of -0.83, -1.55, -0.88 and -1.64, respectively (Figs. 5b, e, f and g). The large  
 320 differences in the distribution of shifts over different ROIs demonstrate that the shifts in the  
 321 along-track direction are dependent on the region. It is interesting to find that ROI 7 still shows  
 322 the smallest StdDev of 0.59 when excluding ROI 5 due to its very small number of patches.  
 323 This indicates that ROI 7 also shows the smallest uncertainty in the along-track direction. And  
 324 this may be associated with its smallest SatZ among all investigated ROIs. When combining  
 325 the results of different ROIs (Fig. 5h), the overall shifts in the along-track direction  
 326 approximately obey a normal distribution, with an average of -0.70 and a standard deviation of  
 327 1.01. Nearly 70% of them are within the range of  $\pm 1$  km, and only a small part (1.5%) show  
 328 values larger than 3 km.

329 Furthermore, it can be stated that the distribution of shifts in the along-track direction is  
 330 less widely spread than that in the across-track direction, demonstrating the smaller uncertainty  
 331 of geocoding in the along-track direction, as indicated by the smaller StdDev values throughout  
 332 these ROIs (Table 2). Moreover, the geolocation errors in the across-track direction are greater  
 333 than the along-track direction (Fig. 5), which is expected due to the applied clock drift  
 334 correction.

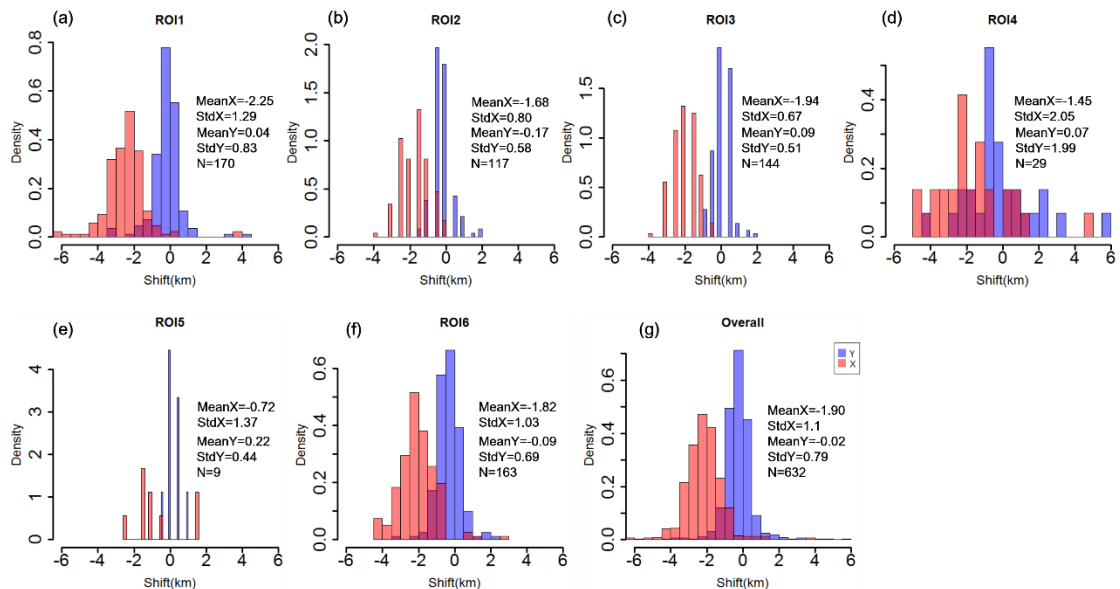
335 **Table 2.** Summary of the results for the scene of NOAA-17. The unit of the shift is km.

ROI	Elevation(m)	Min(X)	Max(X)	Mean(X)	StdDev(X)	Min(Y)	Max(Y)	Mean(Y)	StdDev(Y)	N
1	481	-5	7	-2.18	1.37	-3.5	3.5	-0.18	0.85	170
2	1436	-3.5	5	-0.76	1.19	-4.5	6	-0.83	1.18	115
3	518	-5	1.5	-1.93	1.14	-2.5	1.5	-0.28	0.67	144
4	436	-5	-1	-2.49	1.23	-2.5	1	-0.29	0.80	36
5	543	-3	0	-1.35	0.97	-2	-1	-1.55	0.28	10
6	1094	-7.5	4	-1.33	1.41	-4	3.5	-0.88	1.01	163
7	440	-4.5	0	-1.88	0.77	-3.5	0	-1.64	0.59	121
Overall	/	-7.5	7	-1.69	1.32	-4.5	6	-0.70	1.01	759

336 Similar to the results of NOAA-17, MetOp-A scene mainly present West shifts in the  
 337 across-track direction, indicated by the widely distributed negative values throughout these  
 338 ROIs (Figs. 6a-f). These shifts are basically concentrated around -2, however, the ROIs 2 and  
 339 6 located in the terrain areas, show smaller average shifts (-1.68 and -1.82, respectively) than  
 340 those of ROIs 1 and 3 (-2.25 and -1.94, respectively) over the relatively flat areas. This is  
 341 understandable since the ROIs 2 and 6 are closer to the nadir area (Fig. 1d). And this align with  
 342 the results from NOAA-17, where the influence of SatZ is also stronger than the terrain effect.  
 343 Although the ROIs 5 and 4 show the smallest average shifts (-0.72 and -1.45, respectively) in

344 the across-track direction, their results may be biased due to the smaller number of analyzed  
 345 patches. It is interesting to find that ROI 3, which is almost located in the nadir area, still shows  
 346 the least uncertainty, indicated by the smallest StdDev of 0.67. Furthermore, all ROIs close to  
 347 the nadir area are characterized by small StdDevs (0.8 and 1.03 for ROIs 2 and 6, respectively)  
 348 compared to ROIs located further away from the nadir area (1.29, 2.05, 1.37 for ROIs 1, 4, 5,  
 349 respectively). These results demonstrate that SatZ plays a crucial role in determining the  
 350 uncertainty of the shifts in the across-track direction. This conclusion also agrees with previous  
 351 research conducted by Aguilar et al. (2013). When combining the results of all ROIs (Fig. 6g),  
 352 the shifts approximately follow a normal distribution, with an average of -1.90 and a standard  
 353 deviation of 1.1. Most of the patches (94%) are within the range of  $\pm 3$  km, and nearly 98% of  
 354 them are with shifts less than  $\pm 4$  km.

355 Since ROIs 1-6 on the MetOp-A scene are identical to those on NOAA-17 scene in terms  
 356 of spatial extents, their shifts in the across-track direction are generally comparable. When  
 357 excluding the results of ROIs 4 and 5, the ROIs on the MetOp-A scene generally show larger  
 358 average shifts but smaller StdDevs than the NOAA-17 scene in the across-track direction (see  
 359 Table 2 and 3). However, it does not necessarily mean that the MetOp-A scene has a smaller  
 360 uncertainty than NOAA-17 scene in the across-track direction, because the ROIs on the MetOp-  
 361 A scene are slightly closer to the nadir area than those on the NOAA-17 scene (Figs. 1b and d).  
 362 Given the larger SatZ and the smaller average shifts of NOAA-17 scene, it is reasonable to  
 363 conclude that the NOAA-17 scene shows a slightly better geolocation accuracy than the  
 364 MetOp-A scene in the across-track direction.



365  
 366 **Figure 6.** The distribution of shifts in the across-track (X, represented by red histogram) and along-track  
 367 (Y, denoted as blue histogram) directions over different regions for MetOp-A scene. The unit of the shift  
 368 is km. For histograms, density instead of frequency is labelled in the ordinate.

369 Looking at the shifts in the along-track direction, the MetOp-A scene does not show strong

370 systematic North or South shifts, but rather a general distribution of the shifts around 0 (Figs.  
 371 6a-f). The shifts are generally small within a range of  $\pm 1$  km, with StdDevs less than 0.83  
 372 except for ROI 4. Furthermore, ROIs 2, 3 and 6 that are located close to the nadir area exhibit  
 373 smaller StdDevs than those located further away from the nadir area when excluding ROI 5 due  
 374 to its very small number of patches. This further indicates that SatZ also determines the  
 375 uncertainty of shifts in the along-track direction. When combining the results of all ROIs (Fig.  
 376 6g), the shifts also display a nearly normal distribution, with an average of -0.02 and a StdDev  
 377 of 0.79. Nearly 94% of the shifts are within the range of  $\pm 1$  km and almost all of them (98%)  
 378 are distributed within the range of  $\pm 2$  km. It can be found that the shifts in the along-track  
 379 direction are obviously smaller and more centralized than those in the across-track direction.  
 380 This can be further confirmed by the consistently smaller StdDev values in the along-track  
 381 direction than those in the across-track direction as shown in Table 3.

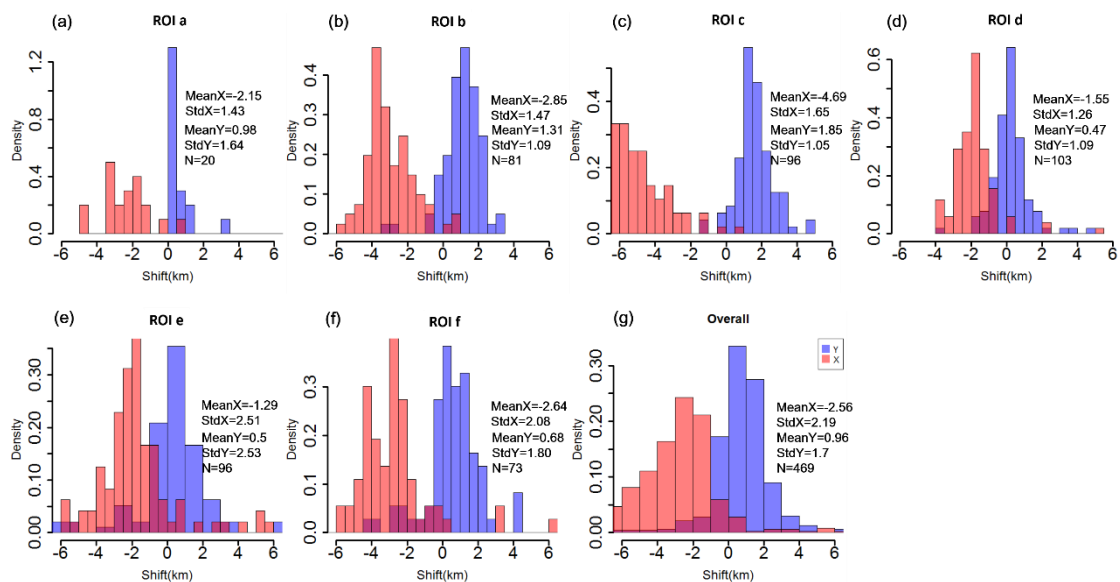
382 **Table 3.** Summary of the results for the scene of MetOp-A. The unit of the shift is km.

ROI	Elevation(m)	Min(X)	Max(X)	Mean(X)	StdDev(X)	Min(Y)	Max(Y)	Mean(Y)	StdDev(Y)	N
1	479	-7	4	-2.25	1.29	-3.5	4.5	0.04	0.83	170
2	1440	-4	0	-1.68	0.80	-1.5	2	-0.17	0.58	117
3	518	-4	-0.5	-1.94	0.67	-1	2	0.09	0.51	144
4	436	-5	5	-1.45	2.05	-4.5	6	0.07	1.99	29
5	540	-2.5	1.5	-0.72	1.37	-0.5	1	0.22	0.44	9
6	1095	-4.5	3	-1.82	1.03	-3.5	2.5	-0.09	0.69	163
Overall	/	-7	5	-1.90	1.10	-4.5	6	-0.02	0.79	632

383 By comparing Figs. 6a-f with Figs. 5a-f, it becomes obvious that large differences exist  
 384 between the shifts in the along-track direction of MetOp-A and NOAA-17 scenes. In the first  
 385 place, systematic South shifts occur on the NOAA-17 scene but not on the MetOp-A scene.  
 386 Secondly, the magnitudes of shifts on the MetOp-A scene are generally smaller than those on  
 387 the NOAA-17 scene, as the former are concentrated around 0 while the latter are concentrated  
 388 around -1. Thirdly, the distribution of shifts is more centralized for the MetOp-A scene  
 389 compared to the NOAA-17 scene, except for ROIs 4 and 5. This can further be proved by the  
 390 smaller StdDev values for MetOp-A (Table 3) than those for NOAA-17 (Table 2). Therefore, it  
 391 can be concluded that the MetOp-A scene shows a better geolocation accuracy and less  
 392 uncertainty than the NOAA-17 scene in the along-track direction.

393 Similar to the scenes of NOAA-17 and MetOp-A, the MetOp-B scene generally shows  
 394 West shifts in the across-track direction, indicated by the predominant occurrence of negative  
 395 values (Figs. 7a-f). Nevertheless, unlike the results for the terrain areas on NOAA-17 and  
 396 MetOp-A scenes, the ROI c located in the terrain area on the MetOp-B scene (Fig. 2a), shows  
 397 the largest shifts throughout these ROIs with an average of -4.69 in the across-track direction.  
 398 Furthermore, the magnitudes of these shifts are characterized by even larger values than 6 km  
 399 (Fig. 7c). This is most probably caused by the combined effect of topography and large SatZ  
 400 (Fig. 2b). Significant terrain effects appear only in the case of SatZ larger than  $40^\circ$  as shown in

401 Fig. 2b. This finding agrees with the previous study by Fontana et al. (2009), who demonstrated  
 402 that the errors in across-track direction result from the intertwined effects of observation  
 403 geometry and terrain elevation. Nevertheless, ROI e that is located in the nadir area (Fig. 2d),  
 404 shows the smallest average shift of -1.29 but the largest standard deviation of 2.51 (Fig. 7e).  
 405 The largest StdDev is attributed to the fact that a considerable number of shifts exhibit values  
 406 of  $\pm 6$  km. As shown in Fig. 2c, the main reason for these large and unstable shifts may be the  
 407 presence of thin clouds or cloud shadows in this region. By comparing the results of ROIs d  
 408 and e with smaller SatZ against ROIs b, c, f with larger SatZ (Figs. 2b and d), it can be stated  
 409 that the shifts with smaller SatZ are generally weaker than those with larger SatZ (Figs. 7b-f).  
 410 When combining the results of all ROIs (Fig. 7g), the MetOp-B scene shows an average shift  
 411 of -2.56 km with a standard deviation of 2.19 in the across-track direction. Only 63% of the  
 412 shifts are distributed within the range of  $\pm 3$  km, and the percentage raises up to 92% within  
 413 the range of  $\pm 5.5$  km.



414

415 **Figure 7.** The distribution of shifts in the across-track (X, represented by red histogram)  
 416 (Y, denoted as blue histogram) directions over different regions for MetOp-B scene. The unit of the shift  
 417 is km. For histograms, density instead of frequency is labelled in the ordinate.

418 Since the extent of the ROIs in the MetOp-B scene are not consistent with those on NOAA-  
 419 17 and MetOp-A scenes, only their overall performances in the across-track direction are  
 420 compared here. By comparing Fig. 7g with Fig. 6g and Fig. 5h, it is obvious that the MetOp-B  
 421 scene shows larger shifts and greater uncertainties than NOAA-17 and MetOp-A scenes in the  
 422 across-track direction. This is partly due to the larger range of SatZ of these ROIs and partly  
 423 due to the worse geolocation accuracy of the MetOp-B scene in the across-track direction.

424 The MetOp-B scene is dominated by North shifts in the along-track direction, indicated  
 425 by the predominantly positive shift values (Figs. 7a-f). It is interesting to find that ROI c, which  
 426 is located at terrain area and with large SatZ, shows the largest shifts with an average of 1.85



427 km in the along-track direction. Given that terrain does not affect the geolocation accuracy in  
 428 the along-track direction, the main cause of the largest shift may be the largest SatZ of ROI c  
 429 among these ROIs. Furthermore, by comparing the results of ROI d and e with those of ROI b,  
 430 c, f, it can be found the shifts of ROIs with smaller SatZ are more concentrated around 0 (Figs.  
 431 7d and e), while the shifts of ROIs with larger SatZ are more widely spread (Figs. 7b, c, and f).  
 432 This manifests that the effect of large SatZ on shifts in the along-track direction cannot be  
 433 neglected. When combining the results of all ROIs, the MetOp-B scene shows shifts with an  
 434 average of 0.96 and a standard deviation of 1.7. Only 52% of the shifts are distributed within  
 435 the range of  $\pm 1$  km, and the percentage raises up to 92% for the range of  $\pm 3$  km.

436 It can be seen that the shifts in the along-track direction are still significantly smaller than  
 437 those in the across-track direction. Furthermore, the uncertainties of the shifts in the along-track  
 438 direction are generally smaller than those in the across-track direction, when excluding the  
 439 results of ROI a due to its limited number of patches (Table 4). This further verifies that after  
 440 removing clock drift errors, the geolocation errors in the along-track direction are generally  
 441 more accurate and with less uncertainties than the across-track direction.

442 **Table 4.** Summary of the results for the scene of MetOp-B. The unit of the shift is km.

ROI	Elevation(m)	Min(X)	Max(X)	Mean(X)	StdDev(X)	Min(Y)	Max(Y)	Mean(Y)	StdDev(Y)	N
a	236	-5	1	-2.15	1.43	0	7	0.98	1.64	20
b	566	-7.5	1	-2.85	1.47	-3.5	3.5	1.31	1.09	81
c	1677	-7.5	1	-4.69	1.65	-1.5	5	1.85	1.05	96
d	406	-4	5.5	-1.55	1.26	-4	5	0.47	1.09	103
e	729	-6	7.5	-1.29	2.51	-7.5	7.5	0.50	2.53	96
f	420	-7.5	6.5	-2.64	2.08	-7	4.5	0.68	1.80	73
Overall	/	-7.5	7.5	-2.56	2.19	-7.5	7.5	0.96	1.70	469

443 The comparison of Fig. 7g with Fig. 6g and Fig. 5h reveals that the MetOp-B scene is  
 444 significantly inferior to the MetOp-A scene in terms of the geolocation accuracy in the along-  
 445 track direction, with the former being concentrated around 1 and the latter around 0.  
 446 Furthermore, the uncertainty of the shifts of the MetOp-B scene (StdDev=1.7) is much larger  
 447 than that of the MetOp-A scene (StdDev=0.79). As for the performance of the MetOp-B scene  
 448 relative to the NOAA-17 scene, it can be found that they are comparable with regard to the  
 449 magnitude as well as the distribution of the shifts in the along-track direction. However, the  
 450 MetOp-B scene shows larger uncertainties than NOAA-17.

451 From the results above, it can be concluded that NOAA-17 and MetOp-A scenes show  
 452 distinct advantages over the MetOp-B scene in both directions. However, the NOAA-17 scene  
 453 is slightly better than the MetOp-A scene in the across-track direction, with average shifts of -  
 454 1.69 for NOAA-17 and -1.90 for MetOp-A, which are both greatly lower than for MetOp-B (-  
 455 2.56). But the MetOp-A scene shows a distinct advantage over NOAA-17 in the along-track  
 456 direction, with an average shift of -0.02 for MetOp-A and -0.7 for NOAA-17, which are both  
 457 lower than for MetOp-B (0.96). In addition to the magnitudes of their shifts, the MetOp-B scene  
 458 also shows larger uncertainties than NOAA-17 and MetOp-A scenes in both directions.

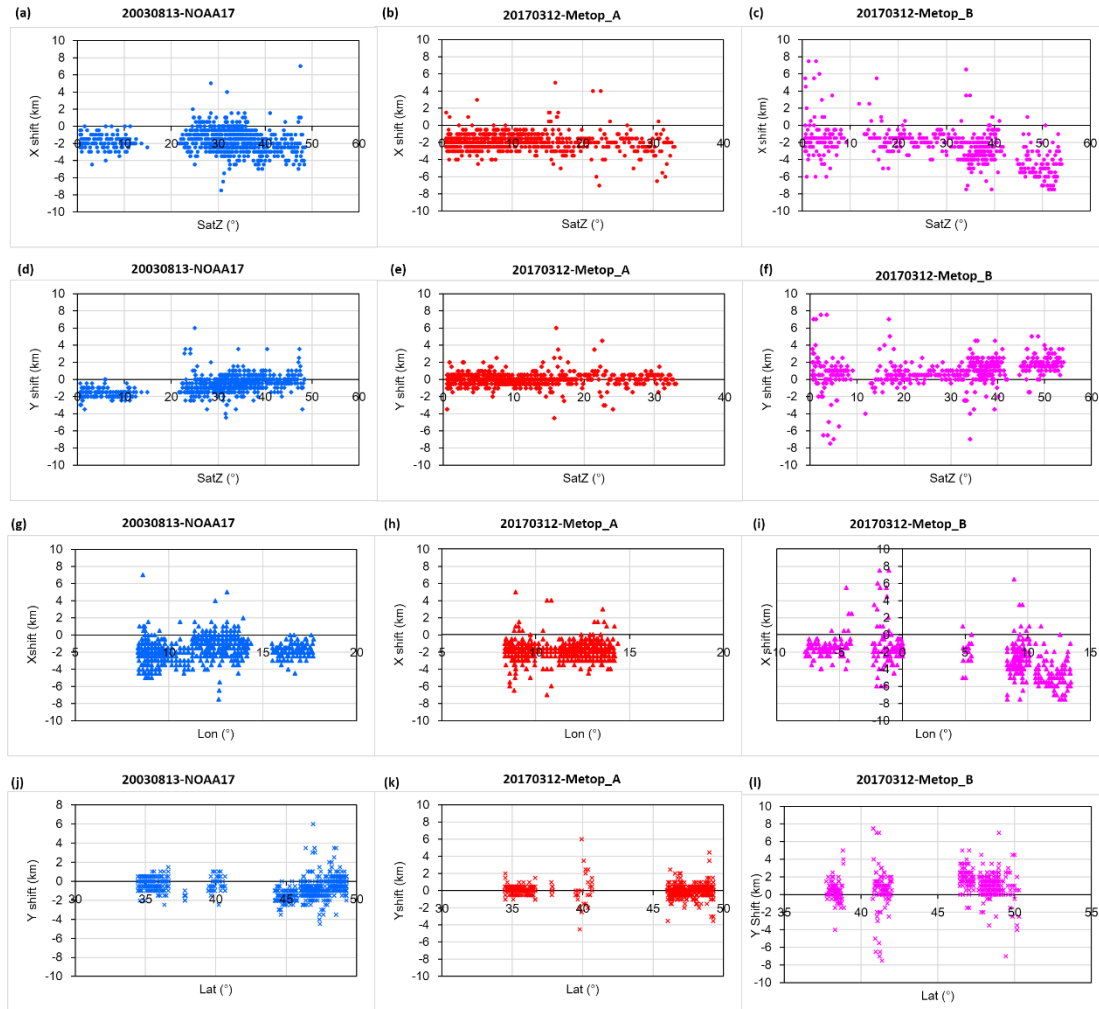
## 459 4.2 The potential influence factors

460 From the above results, it is known that SatZ plays an important role in determining the  
461 geolocation accuracy of the satellite scene. To investigate how and to what extent it influences  
462 the geolocation accuracy, Fig. 8 displays the shifts in both directions as a function of SatZ for  
463 all three satellites. Furthermore, the influences of latitude and longitude on geolocation  
464 accuracy are also explored.

465 As shown in Figs. 8a-c, it can be seen that the shifts in the across-track direction vary  
466 considerably for all SatZ, and this is particularly evident in the results of MetOp-B (Fig. 8c).  
467 This demonstrates that besides the SatZ effects, the geolocation accuracy is also influenced by  
468 other factors. Furthermore, the spread at each fixed SatZ tends to become larger at larger SatZ  
469 (larger than  $20^\circ$ ) (Figs. 8a-b). The large variability of MetOp-B scene shifts at small SatZ (less  
470 than  $20^\circ$ ) (Fig. 8c) is mainly due to the effect of thin cloud or cloud shadow as explained before.  
471 Despite the dispersion of the shifts for all SatZ, it can still be found that the shifts in the across-  
472 track direction do not change much when the SatZ is less than  $20^\circ$  (Figs. 8a-b and Table 5). A  
473 slightly decreasing trend (increasing trend of the magnitude) can be observed from  $20^\circ$  to  $40^\circ$   
474 (Table 5), and becomes more apparent at SatZ larger than  $40^\circ$  (Fig. 8c and Table 5).  
475 Furthermore, it can be found that for small SatZ (less than  $20^\circ$ ) the shifts in the across-track  
476 direction are generally concentrated around 2 km for NOAA-17 and MetOp-A scenes (Figs. 8a-  
477 b). With increasing SatZ, the largest magnitudes of shifts become larger but basically stay  
478 within the range of 4 km for SatZ smaller than  $40^\circ$ . For even larger SatZ (larger than  $40^\circ$ ), the  
479 magnitude of shifts can reach 6 km for NOAA-17 scene and 8 km for MetOp-B scene. From  
480 these results, it can be inferred that the SatZ has a considerable effect on both the magnitude  
481 and uncertainty of the shifts in across-track direction. The larger SatZ generally contributes to  
482 larger shifts and uncertainties in the across-track direction. Furthermore, it can be inferred that  
483 the GAC data with SatZ less than  $40^\circ$  should be preferred in applications.

484 Compared to the shifts in the across-track direction (Figs. 8a-c), the shifts in the along-  
485 track direction show smaller variability at each fixed SatZ (Figs. 8d-f). From Figs. 8d-e, it can  
486 be seen that the shifts in the along-track direction are relatively stable at each level of SatZ for  
487 SatZ smaller than  $15^\circ$ , but becomes more variable for greater SatZ. A similar phenomenon can  
488 be observed in Fig. 8f, where the shifts are relatively stable with SatZ ranging from  $20^\circ$  to  $35^\circ$ ,  
489 but becomes more variable at each level of SatZ with its values larger than  $35^\circ$ . It is noteworthy  
490 that the wide spread of shifts with SatZ less than  $20^\circ$  is mainly caused by cloud contamination.  
491 These results confirm the influence of larger SatZ on the uncertainty of shifts in the along-track  
492 directions. It is interesting to find that the magnitudes of NOAA-17 scene shifts with small SatZ  
493 (less than  $20^\circ$ ) are even larger than those with larger SatZ (larger than  $20^\circ$ ) (Fig. 8d). On the  
494 contrary, the magnitudes of MetOp-B scene shifts with smaller SatZ ( $20$ - $35^\circ$ ) are smaller than  
495 those with larger SatZ (larger than  $35^\circ$ ) (Fig. 8f). Nevertheless, all three sensors have in  
496 common that they do not show clear change with SatZ smaller than  $20^\circ$  for NOAA-17 and

497 smaller than 35° for MetOp-A and MetOp-B (Figs. 8d-f). For larger SatZ than these values,  
 498 shifts exhibit a slightly decreasing trend for NOAA-17 (Fig. 8d) and an increasing trend for  
 499 MetOp-B (Fig. 8f). From these results, it can be stated that the influences of large SatZ on the  
 500 magnitude of shifts in the along-track direction are probably intertwined with other factors.



501  
 502 **Figure 8.** Influence of SatZ on the geolocation accuracy in the across-track (a-c) and along-track (d-f)  
 503 directions. (g-i) and (j-l) describe the influence of longitude and latitude on the geolocation accuracy in  
 504 the across-track and along-track directions, respectively. The left column indicates results of NOAA-17  
 505 (blue), middle for MetOp-A (red), and right for MetOp-B (pink) scenes.

506 **Table 5.** The mean shift for each range of SatZ in the across-track direction. The unit of the shift is km.

SatZ	0°-10°	10°-20°	20°-30°	30°-40°	40°-50°	50°-60°
NOAA-17	-1.84	-1.84	-1.32	-1.66	-2.27	
MetOp-A	-1.87	-1.80	-2.06	-2.62		
MetOp-B	-1.29	-1.45	-1.75	-2.71	-3.95	-4.93

507 For NOAA-17, the shifts tend to be smaller with the longitudinal range of 10°-15° and  
 508 become larger outside this range (Fig. 8g). The MetOp-A scene does not show apparent change  
 509 with longitude between 8° and 15° and neither does MetOp-B within the range between -8° and

510 0° (Fig. 8 h and i, respectively). However, MetOp-B presents a clear decreasing trend (an  
511 increasing trend in magnitude) for longitudes larger than 5°. Given the fact that the latitude of  
512 the nadir area is distributed between 10°-15° for NOAA-17, 8°-15° for MetOp-A, and -8°-0°  
513 for MetOp-B (Figs. 1b and d, Figs. 2b and d), it can be concluded that the influence of longitude  
514 on the shifts in the across-track direction is related to the longitude of nadir area of the satellite,  
515 as it shows almost no influence in the nadir area. The influence increases with the difference of  
516 the longitude relative to that of the nadir area. This is well understandable, as the influence of  
517 longitude is equivalent to that of SatZ in the across-track direction.

518 The variation of the shifts (in the along-track direction) with latitude also depends on the  
519 situation (Figs. 8j-l). The magnitudes of shifts with larger latitude (larger than 45°) are generally  
520 greater than those with smaller latitude (less than 40°) on the NOAA-17 (Fig. 8j) and MetOp-  
521 B scene (Fig. 8l). This is not visible for the MetOp-A scene (Fig. 8k), where the shifts exhibit  
522 almost no change with latitude. This can be attributed to the fact that the clock drift errors are  
523 corrected more thoroughly for MetOp-A satellite than NOAA-17 and MetOp-B satellites.  
524 Furthermore, the MetOp satellites have an on-board stabilization to keep them in the right  
525 position and orientation in orbit compared to the NOAA satellites.

## 526 **5 Conclusions**

527 The geometric accuracy of satellite data is crucial for most applications as geometric  
528 inaccuracy can bias the obtained results. Therefore, the assessment of the geolocation accuracy  
529 is important to provide satellite data of high quality enabling successful applications. In this  
530 study, a correlation-based patch matching method was proposed to characterize and quantify  
531 the AVHRR GAC geo-location accuracy. This method presented here yields significant  
532 advantages over existing approaches and enables achieving a subpixel geo-positioning accuracy  
533 of coarse resolution scenes. It is free from the impact of false detection due to the influence of  
534 mixed pixels, not limited to a certain landmark (e. g. shoreline) and therefore enables a more  
535 comprehensive geometric assessment. This method was utilized to characterize the geolocation  
536 accuracy of AVHRR GAC scenes from NOAA-17, MetOp-A, and MetOp-B satellites.

537 The study is based on several ROIs comprising numerous patches over different land cover  
538 types, latitudes, and topographies. The scenes from these satellites all present West shifts in the  
539 across-track direction, with an average shift of -1.69 km and a StdDev of 1.32 km for NOAA-  
540 17, -1.9 km and 1.1 km respectively for MetOp-A, and -2.56 km and 2.19 km respectively for  
541 MetOp-B. In regard to the shifts in the along-track direction, NOAA-17 generally shows South  
542 shifts with an average of -0.7 km and a StdDev of 1.01 km. By contrast, the MetOp-B mainly  
543 present North shifts with an average of 0.96 km and a StdDev of 1.70 km. The MetOp-A scene  
544 shows a distinct advantage over NOAA-17 and MetOp-B in the along-track direction without  
545 obvious shifts, indicated by the average of -0.02 km and a StdDev of 0.79 km. Generally, the  
546 MetOp-B scene is inferior to NOAA-17 and MetOp-A scenes, with larger shifts and

547 uncertainties in both directions. Despite the variation of shifts due to various factors (e. g. SatZ,  
548 topography), more than 90 percent of the AVHRR GAC data across-track errors are within  $\pm$   
549 3 km for NOAA-17 and MetOp-A, and  $\pm$ 5.5 km for MetOp-B. Along-track errors are within  
550  $\pm$ 2 km for NOAA-17,  $\pm$ 1 km for MetOp-A, and  $\pm$ 3 km for MetOp-B for more than 90  
551 percent of the test data. It is important to note that since these satellites show different shifts,  
552 using the combined data from NOAA-17 and MetOp will result in additional uncertainty in  
553 time series applications.

554 From the results above, it can be found that the geolocation accuracy in the along-track  
555 direction is always higher and with less uncertainties than the across-track direction, which is  
556 consistent with previous related studies. This is understandable since the GAC dataset from the  
557 ESA cloud CCI project has been corrected for clock drift errors, but has no ortho-correction,  
558 which is not feasible due to the onboard sampling characteristics. SatZ plays a decisive role in  
559 determining the magnitude as well as the uncertainty of the shifts in the across-track direction.  
560 Larger SatZ generally induce greater shifts and uncertainties in this direction. The combined  
561 effect of SatZ and topography on geolocation accuracy in the across-track direction has also  
562 been shown. And significant terrain effects appear only in the case of large SatZ ( $>40^\circ$  for this  
563 study). It is important to note that the effect of SatZ on the magnitude and uncertainty of shifts  
564 in the along-track direction is not negligible. But this effect is likely to be intertwined with other  
565 factors. The impact of longitude on the shifts in the across-track direction is equivalent to that  
566 of SatZ, while the effect of latitude is related to the degree of how the clock drift errors are  
567 corrected. It was found that the clock drift errors are more thoroughly corrected for MetOp-A  
568 than NOAA-17 and MetOp-B.

569 Although this assessment was only conducted for a single scene of each satellite, the  
570 highly variable ROIs take the influential factors of geometric accuracy well into account.  
571 Therefore, the presented conclusions are transferable to other regions or seasons. However, it  
572 is noteworthy that this method is not applicable to homogeneous surface (e.g., water, desert),  
573 where the correlations are almost the same in any simulated displacement cases. In general, this  
574 study provides an important preliminary geolocation assessment for AVHRR GAC data. It is a  
575 first step towards a more precise geolocation and thus improves application of coarse-resolution  
576 satellite data. For instance, it identifies the threshold of SatZ under which the GAC data should  
577 be preferred in applications. Furthermore, the CPMM geolocation assessment method proposed  
578 by this study is also applicable to other coarse-resolution satellite data.

## 579 **Data availability**

580 The AVHRR GAC test data in this paper draw on datasets from ESA CCI cloud project  
581 (<http://www.esa-cloud-cci.org/>) where is also the data availability indicated (Stengel et al.,  
582 2017). And the MOD13A1 V006 data can be downloaded via  
583 <https://ladsweb.modaps.eosdis.nasa.gov/> (Didan, 2015).

## 584 **Author contributions**

585 Xiaodan Wu was responsible for the main research ideas and writing the manuscript.  
586 Kathrin Naegeli contributed to the data collection. Stefan Wunderle contributed to the  
587 manuscript organization. All the authors thoroughly reviewed and edited this paper.

## 588 **Competing interests**

589 The authors declare that they have no conflict of interest.

## 590 **Acknowledgments**

591 The authors are grateful to the ESA CCI (Climate Change Initiative) cloud project team  
592 (Dr. Martin Stengel, Dr. Rainer Hollmann) to make the data sets available for this study. This  
593 work was supported by the National Natural Science Foundation of China (41801226).

## 594 **References**

- 595 Aguilar, M. A., del Mar Saldana, M., and Aguilar, F. J.: Assessing geometric accuracy of the  
596 orthorectification process from GeoEye-1 and WorldView-2 panchromatic images, *Int. J. Appl.*  
597 *Earth Obs.*, 21, 427-435, 2013.
- 598 Aksakal, S. K.: Geometric accuracy investigations of SEVIRI high resolution visible (HRV) level  
599 1.5 Imagery, *Remote Sens.*, 5(5), 2475-2491, 2013.
- 600 Aksakal, S. K., Neuhaus, C., Baltasvias, E., and Schindler, K.: Geometric quality analysis of  
601 AVHRR orthoimages, *Remote Sens.*, 7(3), 3293-3319, 2015.
- 602 Alcaraz - Segura, D., Chuvieco, E., Epstein, H. E., Kasischke, E. S., and Trishchenko, A.: Debating  
603 the greening vs. browning of the North American boreal forest: differences between satellite  
604 datasets, *Global Change Biol.*, 16(2), 760-770, 2010.
- 605 Arnold, G. T., Hubanks, P. A., Platnick, S., King, M. D., and Bennartz, R.: Impact of Aqua  
606 misregistration on MYD06 cloud retrieval properties. In *Proceeding of MODIS Science Team*  
607 *Meeting*, Washington, DC, USA, 26–28 January 2010.
- 608 Bennartz, R.: On the use of SSM/I measurements in coastal regions. *J. Atmos. Oceanic Technol.*,  
609 16(4), 417-431, 1999.
- 610 Bicheron, P., Amberg, V., Bourg, L., Petit, D., Huc, M., Miras, B., ... and Leroy, M.: Geolocation  
611 Assessment of MERIS GlobCover Orthorectified Products, *IEEE Trans. Geosci. Remote Sens.*,  
612 49(8), 2972-2982, 2011.
- 613 Cihlar, J., Latifovic, R., Chen, J., Trishchenko, A., Du, Y., Fedosejevs, G., and Guindon, B.:  
614 Systematic corrections of AVHRR image composites for temporal studies, *Remote Sens.*  
615 *Environ.*, 89(2), 217-233, 2004.
- 616 Delbart, N., Le Toan, T., Kergoat, L., and Fedotova, V.: Remote sensing of spring phenology in



617 boreal regions: A free of snow-effect method using NOAA–AVHRR and SPOT–VGT data  
618 (1982–2004), *Remote Sens. Environ.*, 101, 52–62, 2006.

619 Devasthale, A., Raspaud, M., Schlundt, C., Hanschmann, T., Finkensieper, S., Dybbroe, A., ... and  
620 Karlsson, K. G.: PyGAC: an open-source, community-driven Python interface to preprocess  
621 more than 30-year AVHRR Global Area Coverage (GAC) data, 2016.

622 Dietz, A. J., Frey, C. M., Ruppert, T., Bachmann, M., Kuenzer, C., and Dech, S.: Automated  
623 Improvement of Geolocation Accuracy in AVHRR Data Using a Two-Step Chip Matching  
624 Approach—A Part of the TIMELINE Preprocessor, *Remote Sens.*, 9(4), 303, 2017.

625 Didan, K.: MOD13A1 MODIS/Terra Vegetation Indices 16-Day L3 Global 500m SIN Grid V006  
626 [Data set], NASA EOSDIS LP DAAC, doi: 10.5067/MODIS/MOD13A1.006,  
627 <https://ladsweb.modaps.eosdis.nasa.gov/>, 2015.

628 D'Souza, G., and Malingreau, J. P.: NOAA - AVHRR studies of vegetation characteristics and  
629 deforestation mapping in the Amazon Basin, *Remote Sens. Rev.*, 10(1-3), 5-34, 1994.

630 Fontana, F. M., Trishchenko, A. P., Khlopenkov, K. V., Luo, Y., and Wunderle, S.: Impact of  
631 orthorectification and spatial sampling on maximum NDVI composite data in mountain  
632 regions, *Remote Sens. Environ.*, 113(12), 2701-2712, 2009.

633 WMO, I., and UNEP, I.: Systematic observation requirements for satellite-based products for  
634 climate-Supplemental details to the satellite-based component of the “Implementation Plan for  
635 the Global Observing System for Climate in Support of the UNFCCC”[J]. Technical Report  
636 GCOS-107, WMO/TD No 1338, 2006.

637 Han, Y., Weng, F., Zou, X., Yang, H., and Scott, D.: Characterization of geolocation accuracy of  
638 Suomi NPP advanced technology microwave sounder measurements. *J. Geophys. Res. Atmos.*,  
639 121(9), 4933-4950, 2016.

640 Hoffman, L. H., Weaver, W. L., and Kibler, J. F.: Calculation and accuracy of ERBE scanner  
641 measurement locations, NASA Tech. Pap. Rep. NASA/TP-2670, 34 pp., NASA Langley  
642 Research Center, Hampton, Virginia, 1987.

643 Hollmann, R., Merchant, C., Saunders, R., Downy, C., Buchwitz, M., Cazenave, A., Chuvieco, E.,  
644 Defourny, P., Leeuw, G. de, Forsberg, R., Holzer-Popp, T., Paul, F., Sandven, S.,  
645 Sathyendranath, S., Roozendaal, M. van, and Wagner W.: The ESA Climate Change Initiative:  
646 satellite data records for essential climate variables, *B. Am. Meteorol. Soc.*, doi:  
647 10.1175/BAMS-D-11-00254.1, 2013.

648 Hori, M., Sugiura, K., Kobayashi, K., Aoki, T., Tanikawa, T., Kuchiki, K., ... and Enomoto, H.: A  
649 38-year (1978–2015) Northern Hemisphere daily snow cover extent product derived using  
650 consistent objective criteria from satellite-borne optical sensors, *Remote Sens. Environ.*, 191,  
651 402-418, 2017.

652 Khlopenkov, K. V., Trishchenko, A. P., and Luo, Y.: Achieving subpixel georeferencing accuracy in  
653 the Canadian AVHRR processing system, *IEEE Trans. Geosci. Remote Sens.*, 48(4), 2150-  
654 2161, 2010.

655 Kidwell, K. B.: NOAA Polar Orbiter Data (POD) User's Guide, November 1998 revision, 1998.

656 <http://www2.ncdc.noaa.gov/docs/podug/>

657 Lee, T. Y., and Kaufman, Y. J.: Non-Lambertian effects on remote sensing of surface reflectance and  
658 vegetation index, *IEEE Trans. Geosci. Remote Sens.*, 24, 699–708, 1986.

659 Moreno, J. F., and Melia, J.: A method for accurate geometric correction of NOAA AVHRR HRPT  
660 data, *IEEE Trans. Geosci. Remote Sens.*, 31(1), 204-226, 1993.

661 Moulin, S., Kergoat, L., Viovy, N., and Dedieu, G.: Global-scale assessment of vegetation  
662 phenology using NOAA/AVHRR satellite measurements, *J. Climate*, 10, 1154–1170, 1997.

663 Pouliot, D., Latifovic, R., and Olthof, I.: Trends in vegetation NDVI from 1 km AVHRR data over  
664 Canada for the period 1985–2006, *Int. J. Remote Sens.*, 30, 149–168, 2009.

665 Rosborough, G. W., Baldwin, D. G., and Emery, W. J.: Precise AVHRR image navigation, *IEEE*  
666 *Trans. Geosci. Remote Sens.*, 32(3), 644-657, 1994.

667 Stengel, M., Stapelberg, S., Sus, O., Schlundt, C., Poulsen, C., Thomas, G., Christensen, M.,  
668 Carbajal Henken, C., Preusker, R., Fischer, J., Devasthale, A., Willén, U., Karlsson, K.-G.,  
669 McGarragh, G. R., Proud, S., Povey, A. C., Grainger, R. G., Meirink, J. F., Feofilov, A.,  
670 Bennartz, R., Bojanowski, J. S., and Hollmann, R.: Cloud property datasets retrieved from  
671 AVHRR, MODIS, AATSR and MERIS in the framework of the Cloud\_cci project, *Earth Syst.*  
672 *Sci. Data*, 9, 881-904, <https://doi.org/10.5194/essd-9-881-2017>, 2017.

673 Stengel, M., Sus, O., Stapelberg, S., Schlundt, C., Poulsen, C., Hollmann, R.: ESA Cloud Climate  
674 Change Initiative (ESA Cloud\_cci) data: Cloud\_cci AVHRR-AM L3C/L3U  
675 CLD\_PRODUCTS v2.0, Deutscher Wetterdienst (DWD),  
676 [https://doi.org/10.5676/DWD/ESA\\_Cloud\\_cci/AVHRR-AM/V002](https://doi.org/10.5676/DWD/ESA_Cloud_cci/AVHRR-AM/V002), 2017

677 Stöckli, R., and Vidale, P. L.: European plant phenology and climate as seen in a 20 year AVHRR  
678 land-surface parameter dataset, *Int. J. Remote Sens.*, 25, 3303–3330, 2004.

679 Takagi, M.: Precise geometric correction for NOAA and GMS images considering elevation effects  
680 using GCP template matching and affine transform, *Proceedings of SPIE Conference on*  
681 *Remote Sensing, Image and Signal Processing for Remote Sensing IX*, pp.132-141, Vol. 5238,  
682 Barcelona, Spain, 2004.

683 Van, A., Nakazawa, M., and Aoki, Y.: Highly accurate geometric correction for NOAA AVHRR  
684 data, 2008.  
685 [http://cdn.intechopen.com/pdfs/10391/InTech%20Highly\\_accurate\\_geometric\\_correction\\_for](http://cdn.intechopen.com/pdfs/10391/InTech%20Highly_accurate_geometric_correction_for_noaa_avhrr_data.pdf)  
686 [noaa\\_avhrr\\_data.pdf](http://cdn.intechopen.com/pdfs/10391/InTech%20Highly_accurate_geometric_correction_for_noaa_avhrr_data.pdf)

687 Wang, L., Tremblay, D. A., Han, Y., Esplin, M., Hagan, D. E., Predina, J., Suwinski, L., Jin, X., and  
688 Chen, Y.: Geolocation assessment for CrIS sensor data records. *J. Geophys. Res. Atmos.*,  
689 118(22), 12-690, 2013.

690 Wolfe, R. E., Nishihama, M., Fleig, A. J., Kuyper, J. A., Roy, D. P., Storey, J. C., and Patt, F. S.:  
691 Achieving sub-pixel geolocation accuracy in support of MODIS land science, *Remote Sens.*  
692 *Environ.*, 83(1-2), 31-49, 2002.

693 Wolfe, R. E., Lin, G., Nishihama, M., Tewari, K. P., Tilton, J. C., and Isaacman, A. R.: Suomi NPP  
694 VIIRS prelaunch and on-orbit geometric calibration and characterization, *J. Geophys. Res.*

